Inorganic Chemistry

pubs.acs.org/IC

Article

A Single Source, Scalable Route for Direct Isolation of Earth-Abundant Nanometal Carbide Water-Splitting Electrocatalysts

Edward T. Nguyen, Isabella A. Bertini, Amanda J. Ritz, Robert A. Lazenby, Keyou Mao, James R. McBride, Alexzandra V. Mattia, Jason E. Kuszynski, Samuel F. Wenzel, Sarah D. Bennett, and Geoffrey F. Strouse*

Cite This: *Inorg. Chem.* 2022, 61, 13836−13845

Read Online

ACCESS | Metrics & More | Article Recommendations | Supporting Information

ABSTRACT: Single-phase M_xCs (M = Fe, Co, and Ni) were prepared by solvothermal conversion of Prussian blue single source precursors. The single source precursor is prepared in water, and the conversion process is carried out in alkylamines at reaction temperatures above 200 °C. The reaction is scalable using a commercial source of Fe-PB. High-resolution transmission electron microscopy, X-ray photoelectron microscopy, and powder X-ray diffraction confirm that carbides have thin oxide termination but lack graphitic surfaces. Electrocatalytic activity reveals that Fe_3C and Co_2C are oxygen evolution reaction electrocatalysts, while Ni_3C is a bifunctional [OER and hydrogen evolution reaction (HER)] electrocatalyst.

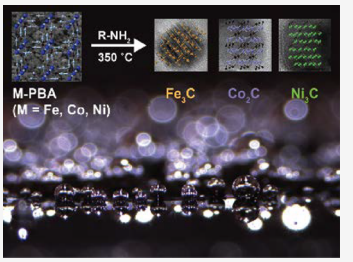

INTRODUCTION

Electrocatalytic water splitting, which consists of the oxygen evolution reaction (OER) at the anode and the hydrogen evolution reaction (HER) at the cathode, is inefficient mainly to kinetic barriers in the OER. Stored hydrogen and oxygen, which can be generated from water splitting reactions powered by sustainable energy sources, have utility in powering fuel cells. While platinum group metals have shown superior performance in both OER and HER, the scarcity of these materials is a liability for long-term commercial applications in water-splitting devices.[1,2] For development of water-splitting devices, areas of interest include the development of bifunctional HER and OER catalysts and earth-abundant catalysts for low-cost production.[3−8] The targeted combined OER and HER overpotentials for a solar water-splitting device operating at 10% efficiency are less than 0.45 V, although it is worth noting that reported electrocatalysts typically do not meet this criteria.[3] New earth-abundant materials, particularly high surface area nanomaterials, that exhibit low overpotentials and high stability are critical to enhance the commercial viability of water splitting, with implications for more efficient fuel cell technology.

The M-Xide (M = transition metal (TM), X = O, C, N, P, S, Se, Te, B) family has been identified as potential catalysts for water-splitting applications.[4] Within this family, the metal carbide family is particularly interesting because of the reported stability and low overpotential.[5−16] In metal carbides, the presence of stacking faults may enhance electrocatalytic activity, reflecting the impact of local disorders on electron density.[8,17−19] Mullins and coworkers reported that Co_3C nanoparticles when calcined to Co_xC exhibit OER activity, but surface oxidation was reported. The study suggested that better OER activity arises from combining the high activity of amorphous cobalt oxide with the high electron density of cobalt carbide.[20] The catalytic activity for first-row TM carbides is dependent on the isolated carbide phase, for instance, in Fe[21] and Co[4], M_2C and M_3C are reported to be catalytically active surfaces, while Ni_3C and NiC[10,22−24] are promising water-splitting precatalysts. The reported overpotentials vary with the synthetic strategy, likely reflecting the ease of carbon migration and presence of multiphase carbide isolation. The presence of mixed phases limits the insight that can be gained on the effectiveness of single-phase carbides for OER and HER.[16,25,26]

In the literature, there are multiple synthetic routes to prepare metal carbide nanocrystals including high temperature decomposition routes of molecular precursors,[14,20,27−29] carburization of metals and metal oxides,[30,31] and the recent demonstration of the thermal conversion of a metal organic framework or Prussian blue analogue (PBA) as single source precursors to the desired carbide.[10,32−36] While the use of high temperature $M(CO)_6$ reactions to produce metal carbide precatalysts is reasonable in the laboratory,[6,14,20,27] a synthetic route utilizing a single source precursor would be advantageous in the development of scalable and sustainable synthesis for industrial applications.[37] PBAs can be converted to carbides and metals via calcining powders or solvothermally.[11,38−43]

Received: May 18, 2022
Published: August 25, 2022

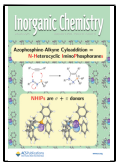

https://doi.org/10.1021/acs.inorgchem.2c01713
Inorg. Chem. 2022, 61, 13836−13845

Researchers have shown pure phase carbides are isolable in Ni and Fe, but the isolated particles are insoluble and embedded in a carbonaceous layer.[24,44]

In this manuscript pure phase, octadecylamine-passivated Fe_3C, Co_2C, and Ni_3C nanocrystal carbides are prepared using a high temperature, solvothermal conversion of the parent PBA in octadecylamine at 350 °C. In the present study, the ability to directly isolate a single-phase carbide that is soluble in organic solvents as the final product of a solvothermal reaction is demonstrated. Conversion of a 51.7 ± 14.7 nm Fe-PB produces a 25 ± 16 nm Fe_3C ($P6_322$); a 171.3 ± 51.4 nm Co-PBA mesocrystal yields 3.1 ± 0.7 nm Co_2C nanocrystals (Pmnn); and 193.5 nm ± 77.3 nm Ni-PBA produces a 64 ± 35 nm Ni_3C nanocrystal (R-3cH). Evidence of the pure phase Fe, Co, and Ni carbides are demonstrated by whole pattern fitting of powder X-ray diffraction (pXRD), transmission electron microscopy (TEM) fringe analysis, and X-ray photoelectron spectroscopy (XPS) data. pXRD reveals that the samples are single-phase carbides with no evidence of oxide or multiple carbide phases. However, TEM fringe analysis coupled to XPS confirm the presence of oxides in the nanocarbides. The surface termination of the Co_2C is assigned to a Co_3O_4 spinel based upon TEM d-spacing and pre vs post sputtered XPS samples. Notably, a crystalline oxide is not observed post- or presputtering in pXRD. Additionally, no identifiable oxide is observed on the iron or nickel high-resolution TEM (HRTEM) images.

The nanocarbides operate as bifunctional catalysts in alkaline conditions, albeit the HER overpotential for all carbides is larger than the target for water-splitting and fuel cell applications.[3] Under acidic conditions, Ni_3C has an overpotential of −0.412 V, which is within the desired range. The Fe, Co, and Ni metal carbides exhibit OER overpotentials of 0.576, 0.423, and 0.503 V at a current density of 10 mA cm^{-2} for geometric area normalized overpotentials, respectively. Electrochemically active surface area (ECSA)-calculated OER overpotentials for Co and Ni metal carbides gave overpotentials of 0.451 and 0.563 V, respectively. Fe_3C is unstable under OER conditions (maximum current density of 7 mA cm^{-2} at 1.8 V), while Co_2C and Ni_3C exhibit prolonged electrochemical stability (<2% increase in overpotential after 100 cycles).

The study demonstrates that solvothermal PBA conversion to the carbide is a facile conversion route. The PBA precursor allows the single source precursor to be prepared in water and converted with no evidence of free cyanide after conversion to the carbide, providing a sustainable and earth-friendly methodology. The demonstration of reaction scalability of Fe_3C from commercially sourced Fe-PB (reactions demonstrated at five-fold and fifty-fold) demonstrates the flexibility of the route in preparing materials for large-scale catalytic studies. The developed synthetic conversion route from PBA to carbide is potentially extendable to a wide range of binary[45] and ternary metal carbides,[46] opening the possibility to develop a robotic, library of synthetic strategies to target the preparation and analysis of catalytic activity for first-row TM carbides. The flexibility of the route reflects the abundance of PBA permutations reported in the literature.[47] The facile route to carbides fits into the larger effort in nano- and microscale carbide investigations for the CO_2 reduction reaction, HER, OER, and Fischer−Tropsch process.[5,13,27,30,37,48−50]

RESULTS AND DISCUSSION

Isolation of Single-Phase TM-Nanocarbides. Reaction of M-PBA (M = Fe, Co, Ni) cubes in octadecylamine at 350 °C for 1 h results in isolation of 25 ± 16 nm Fe_3C from 51.7 ± 14.7 nm Fe-PB, 3.1 ± 0.7 nm pure-phase Co_2C from 171.3 ± 51.4 nm Co-PBA, and a 64 ± 35 nm Ni_3C from a 193.5 nm ± 77.3 nm Ni-PBA platelet (plate thickness 29 ± 12.2 nm). The nanocrystal size was analyzed by TEM for ∼250 nanocrystals, with the histograms available in the Supporting Information (Figure S1). The isolated nanocarbides can be solvated in nonpolar solvents, precipitated by cosolvent addition, and purified on a size-exclusion resin.[51] No free cyanide is observed in the reaction following conversion to the metal carbide (Figure S2).

In Figure 1, characterization data are shown for the conversion of the M-PBA (M = Fe, Co, and Ni) to M_xC (x = 2 (Co), x = 3 (Fe, Ni)). Fe_3C was identified with pXRD pattern fitting to the Fe_3C card, PDF # 01-089-2005. In the Fe_3C sample, the d-spacing is 2.99 Å, indexable to the (1−11) of the Fe_3C. The Fe_3C sample shows significant stacking faults. Co_2C nanocrystals assignable to PDF# 01-072-1369 based on whole-pattern fitting of the pXRD and HRTEM fringe analysis, with a d-spacing of 2.22 Å, indexable to the (020) of the Co_2C. In the Co_2C, TEM imaging in bright field and dark field reveal a Co_2C core (bright, 2.22 Å (020) and 2.42 Å (110)) and a surface Co_3O_4 (dark, 2.8 Å (220)) (Figures S3 and S4). The pXRD pattern is indexed to the Ni_3C card, PDF # 01-072-

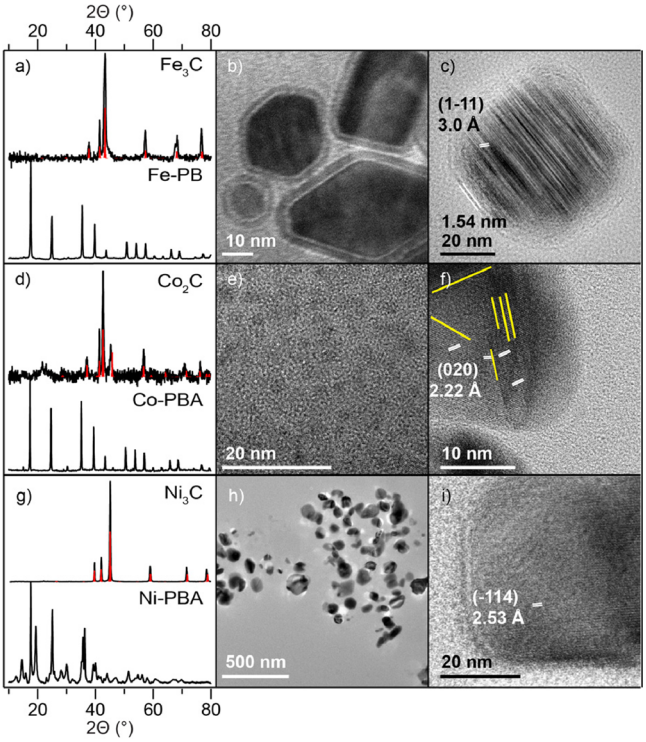

Figure 1. pXRD data. (a) Iron carbide and Iron PB sample, red line indicates Fe_3C reference card positions, (d) Cobalt carbide and Co-PBA, red line indicates Co_2C reference card positions, and (g) Nickel and Ni-PBA, red line indicates Ni_2C reference card positions. TEM images of the (b) Fe_3C, (e) Co_2C, and (h) Ni_3C dispersible nanocrystals. HRTEM of (c) Fe_3C with assignable fringe to (1−11) and carbon shell of 1.54 nm, (f) Co_2C with assignable fringe to (020), and (i) Ni_3C with assignable fringe to (−114).

https://doi.org/10.1021/acs.inorgchem.2c01713
Inorg. Chem. 2022, 61, 13836−13845

1467. HRTEM allows assignment of d-spacing of 2.53 Å assignable to the (−114) Ni_3C. No identifiable stacking faults are observed in the Ni_3C TEM. Higher resolution fringe analysis is available in the Supporting Information, S5−S7).

The pXRD spectra indicate that the carbides are isolated as single-phase nanocarbides without the presence of oxides or mixed carbide phases. Fringe analysis of TEM images reveal well-resolved glide planes in Fe, and Co, but not Ni metal carbides. Characterization data for the M-PBA starting materials are available in the Supporting Information (Fe, Co, and Ni are Figures S8−S10, respectively).

In the TEM images of Fe_3C (Figure 1c) and Co_2C (Figure 1f), strain and stacking faults are clearly present along the (1−11) and (020) planes, respectively. The distance between Co_2C stacking faults was measured to be 1.2 nm, with a grain size measured to be less than 10 nm. Inspection of the Fe_3C stacking faults was measured to be 2.2 nm, with the grain size measured to be greater than 20 nm. Measuring the angle between the fringes on either side of the stacking fault gives angles between 140−152° (Co_2C) and 140−156° (Fe_3C), consistent with the existing literature on metal nanocrystals with stacking fault errors.[52,53] In Figure 1f, the stacking faults are denoted in yellow for clarity. In the Supporting Information, the stacking faults and angles are fully annotated (Figures S5 and S6).

In addition to the presence of stacking faults, a low z-contrast halo is observed. The halo may arise from excess ligand, carbon shelling as previously reported or EM beam damage resulting in ligand polymerization or carbon diffusion out of the nanocarbides. The earlier literature has suggested that a graphitic carbon shell is formed following PBA thermal decomposition, as evidenced by Raman spectroscopy and fringe analysis in the TEM.[24,39,44] The carbon solubility in metal carbides is Fe > Ni > Co based on interstitial formation energies,[54] which is in reasonable agreement with halo thickness in the TEM image, suggesting a carbon layer. Raman measurements on the samples do not show characteristic d and g bands, indicating that the halo is likely amorphous carbon (Figure S11).

In the Fe_3C and Ni_3C nanocarbides, the halo is observed to grow in thickness with increased EM imaging time, suggesting that beam damage may lead to carbon diffusion from the nanocrystal (Figure S12). During imaging of Fe_3C, the halo increases from 9.67 nm (t = 0) to 11.83 nm (t = 2 min), (Figure S13), coupled to changes in the strain boundary and stacking fault distribution. Closer inspection of the Fe_3C TEM image though shows a d-spacing in the halo of 2.4 Å that may be due to the surface growth of single-walled carbon nanotubes, as previously observed; however, the lack of d and g bands suggests that the percentage of graphitic or amorphous is small, which may be extruded to the solvent during the reaction.[55,56] The formation and subsequent loss of carbon nanotubes at the iron carbide surface is not surprising as it has been reported that carbon can fold into iron and nickel and be extruded.[57−62]

To distinguish the carbide core from the amorphous surface, XPS analysis of the iron, cobalt, and nickel carbide was performed as a function of the time of Ar^+ ion etching. Survey XPS spectra (Figures S14 and S15) and a comprehensive list of XPS binding energies (Tables S1 and S2) are provided in the Supporting Information. In Figure 2, the metal $2p_{3/2}$ and $2p_{1/2}$ XPS features are shown comparing the signal prior and post Ar^+ etching. At t = 0, the XPS data observes features assignable

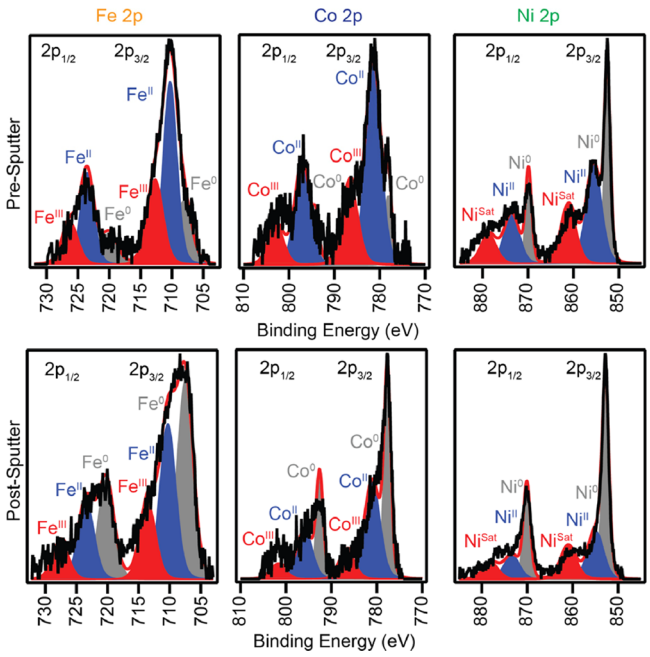

Figure 2. XPS of the Fe, Co, and Ni $2p_{3/2}$ and $2p_{1/2}$ before and after sputtering. Blue and red peaks represent M(II/III) and Ni(Satellite/II), while gray peaks represent M^0.

to Co(0, II, III),[63] Fe(0, II, III), and Ni(0, II, Satellite).[64] Following Ar^+ sputtering, the M(0) feature dominates the spectra. The M(II) and M(III) features reduce in intensity with increasing sputtering time, suggesting the species is associated with the nanocrystal surface, while the M(0) is associated with the metal carbide core. Based on the literature, the observed M(0) feature is assigned to a metal carbide.[49] In Figure 3, the C1s spectra for the M_xC nanocarbides are shown. In the spectra, adventitious carbon (C−C 284.8 eV, C−O−C 286 eV) and a small feature assignable to a metal carbide M−C bond (282 eV) are observed prior to sputtering. Continuous Ar^+ sputtering of the samples shows a reduction of the adventitious carbon and an increase in the M−C carbide, consistent with the M $2p_{3/2,\ 1/2}$ spectra. The spectra may suggest that the M(II/III) oxidation states observed prior to etching are due to surface oxide, consistent with darkfield TEM imaging (Figure S1). As suggested by Mullins and co-workers, the presence of an amorphous oxide generates M(II/III) XPS features.[20] Because TEM shows an amorphous region, the presence of an oxide can be evaluated by the inspection of the O1s data pre- and postsputtering. Postsputtering the Fe, Co, and Ni carbides shows a loss of O1s at 532 and 530 eV with an increase in the 528 eV feature. Based on the previous literature, the 532 and 523 features are assignable to either a C−O or M−O bond,[65] while the 528 eV feature is a lattice oxygen, O^{2-}.[66]

To ensure the oxide observed in the XPS data postsputtering is not an oxide layer, comparison of the pXRD patterns for pre- and postsputtered Fe, Ni, and Co carbide is compared in Supporting Information Figure S16, with no evidence for crystalline oxides, suggesting that the oxide layer is thin. The correlated appearance of M−C and M−O XPS features, postsputtering, suggests the inclusion of MO species within the lattice. The increase in the 528 eV feature with sputtering time, coupled to the lack of an identifiable oxide in pXRD or TEM images, suggests that these are local inclusions present as

https://doi.org/10.1021/acs.inorgchem.2c01713
Inorg. Chem. 2022, 61, 13836−13845

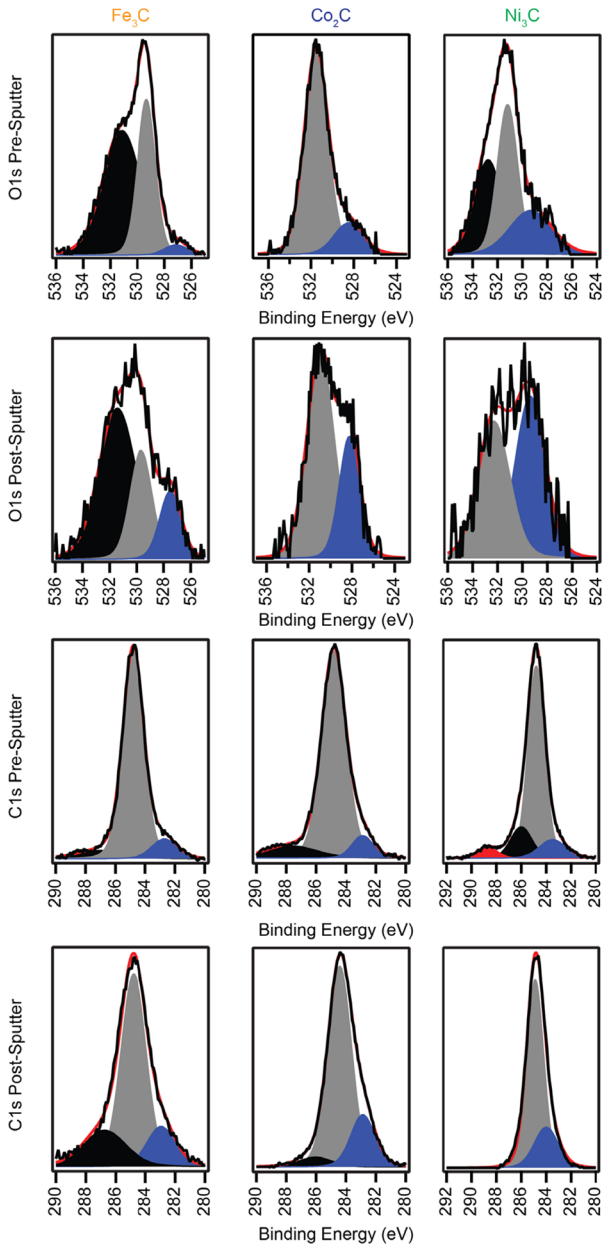

Figure 3. XPS of the Fe, Co, and Ni O1s and C1s before and after sputtering. In the O1s, black peaks represent the C−O, gray represents the M−O, and blue represents O^{2-}. In the C1s, black represents the C−O, gray represents C−C, and blue represents M−C.

defects in the isolated carbide. Whether the appearance of M(II/III) features and MO features presputtering is reflective of ligand binding, an amorphous oxide, or a spinel termination is not conclusive.

The scalability of the reaction was assessed using commercial Fe-PB with reactions carried out up to 2.5 g of Fe-PB in 300 g of octadecylamine yielding 900 mg of Fe_3C, Figure 4. As observed in pXRD, the Fe_3C phase is maintained at all reaction quantities. The demonstration of translatability and scalability has potential significance for preparing hardened materials and precatalysts for the OER and carbon dioxide reduction reaction.

Electrochemical Activity Toward OER. The electrocatalytic activity and stability was demonstrated for the isolated TM-carbides, as shown in Figure 5. Visible evidence of O_2

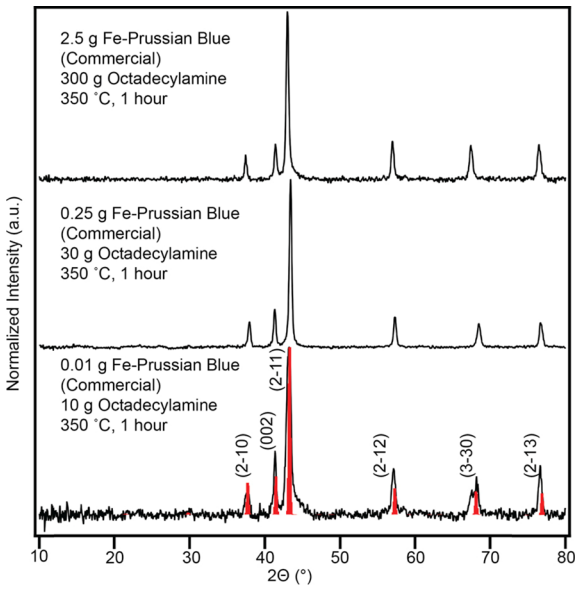

Figure 4. Demonstration of scalability for commercial Fe-PB from a 0.01 g (10 g solvent) to 2.5 g (300 g solvent) synthesis, allowing the isolation of 25 ± 16 nm Fe_3C nanocrystals.

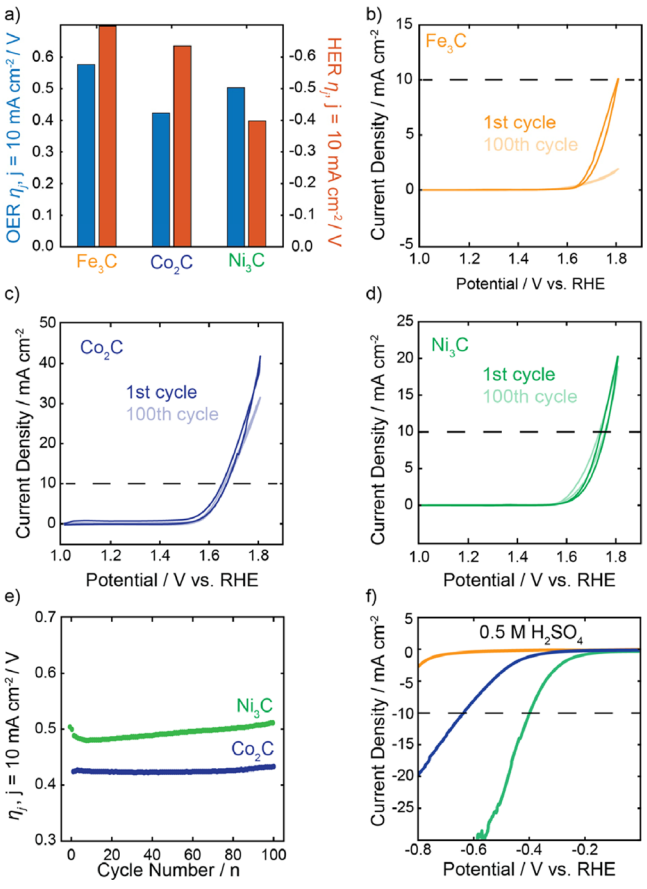

Figure 5. (a) Summary of overpotentials measured at 10 mA cm^{-2} for the OER (alkaline) and HER (acidic) of the nanocarbides. OER activities of (b) Fe_3C, (c) Co_2C, and (d) Ni_3C carbides in 1 M KOH. (e) Electrochemical stability measurements of Ni_3C (green) and Co_2C (purple) up to 100 CV cycles. (f) HER activities of Fe_3C, Co_2C, and Ni_3C in acidic conditions.

https://doi.org/10.1021/acs.inorgchem.2c01713
Inorg. Chem. 2022, 61, 13836−13845

production at the glassy carbon electrode coated with Co_2C (90% Nafion, 10% Co_2C by weight) at 1.6 V vs RHE is observable in the video clip provided in the Supporting Information (Figure S17, Video S1).

For characterization of metal carbides as efficient electrocatalysts, overpotentials were extracted at a benchmark current density of 10 mA cm^{-2}.[3] The electrocatalytic activity toward the OER of metal carbides followed the order Fe < Ni < Co, according to their respective geometric area-normalized overpotentials (at 10 mA cm^{-2}) of 0.576, 0.503, and 0.423 V, with maximum current densities of 10, 42, and 19 mA cm^{-2} observed at 1.8 V. The observed overpotential for the best-performing OER Co_2C electrocatalyst is similar to the reported overpotential for Co_3C (0.455 V).[20] The observed Ni_3C exhibits a higher overpotential compared to a value obtained from the literature (0.500 vs 0.323 V).[24] The lower overpotential for the earlier study is attributable to the earlier sample being a mixed carby-nitride.[24] The observed OER overpotential for Fe_3C is lower than that previously reported.[67] Comparison of the PBA-based metal carbide electrocatalysts to other Fe, Ni, and Co metal X-ides reported in the literature is provided in the Supporting Information (Table S5). It is worth noting, obtaining a meaningful comparison is somewhat complicated by the various methods in which potential catalyst samples are prepared, the range of mass loadings that are used and whether the specific activity of the electrocatalyst is used, which accounts for the electrochemical surface area. In particular, for this last point, using the geometric surface area to calculate current density does not consider changes in microscopic surface area between the samples. For example, electrocatalysts that are supported on Fe or Ni foam electrodes likely have greatly enhanced surface areas, so using the geometric surface may not be a reliable comparison to electrodes supported on polished disk substrates.

The specific activity of these materials is better analyzed through analysis of the ECSA estimated from the electrochemical double layer capacitance for each catalytic surface from the cyclic voltammograms (CV). The ECSA was used to calculate current density for OER/HER because the geometric surface area does not consider changes in the microscopic surface area between the samples. When determining overpotentials from current density for the OER calculated with the ECSA, only the Ni (0.563 V) and Co (0.451 V) metal carbides achieved the benchmarking standard current density of 10 mA cm^{-2} in the potential range of the voltammogram. Fe carbide reached a maximum current density of 7 mA cm^{-2}, observed at 1.8 V.

To provide a semiquantitative analysis of the electrochemical kinetics for electrocatalytic OER, Tafel plots were extracted from the voltammogram of each metal carbide (Figure S18). The resulting linear Tafel slopes, obtained from the low overpotential onset region of the voltammograms, for carbides of Fe, Ni, and Co were 165, 112, and 145 mV dec^{-1}, respectively. These data indicate that OER occurs via a $1e^-$ transfer rate-determining step (~120 mV dec^{-1}),[68] and the Ni carbide has the highest mechanistic efficiency.

The electrochemical stability for Fe_3C, Co_2C, and Ni_3C was assessed over time using repetitive CVs for 100 cycles (4.5 h), with the 1st and 100th CV shown for comparison (Figure 5b,e). The repetitive CV cycling method was chosen to assess stability as it provides testing conditions closest to industrially relevant applications.[69] The Fe_3C decays significantly in OER activity, no longer achieving a current density of 10 mA cm^{-2} after seven CV cycles.

The PBA-grown Co_2C and Ni_3C catalysts are observed to be robust over 100 CV cycles, with the CVs from the 1st to 100th cycle closely overlapping and a < 2% increase of overpotential (η_j, j = 10 mA cm^{-2}) measured over time (Figure 5e). The observed stability is surprising when compared to the report of Mullins for Co_3C where a rapid increase in overpotential was observed over 150 successive scans and ascribed to oxide conversion of the metal carbide.[20]

In Figure 6, pXRD and XPS analysis on post OER samples were performed to assess the growth of an oxide surface for the

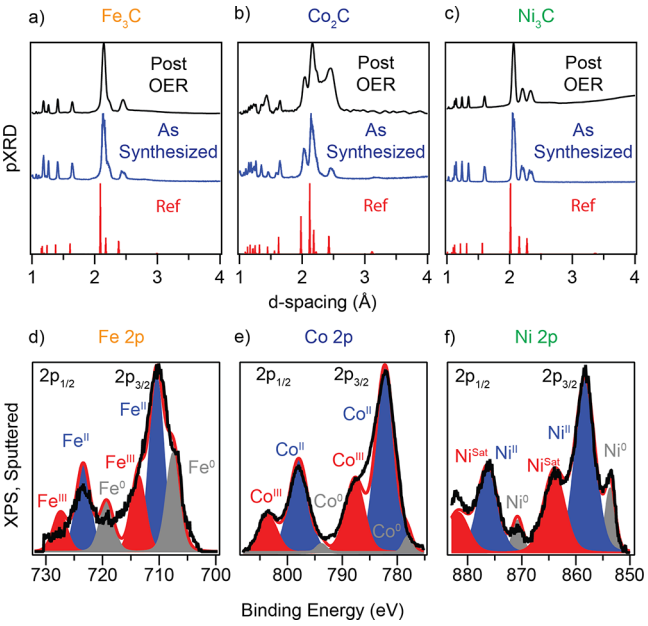

Figure 6. Characterization of Fe, Co, and Ni metal carbides post OER via pXRD (a–c). (d–f) XPS of the M 2p of the Fe, Co, and Ni metal carbides after sputtering.

Co, Ni, and Fe (Survey Spectra S19 and S20; Table of Binding Energies and FWHM S3, S4). The pXRD data do not exhibit identifiable oxide features, suggesting that the catalyst core is not converted to an oxide during OER, as suggested by Mullins. XPS analysis on the post OER samples indicates that oxide formation does occur at the surface during OER, with the oxide thickness following the trend Fe > Co > Ni. Sputtering data obtained at different sputtering times confirm the trend and are available in Supporting information (Figures S21 and 22). The post-OER data confirm Mullins observation of oxide growth, which influences long-term OER activity.

The high stability for the PBA derived Co_2C when compared to the report on Co_3C may suggest either the 2:1 phase is more stable under alkaline conditions than the 3:1 phase or perhaps the presence of spinel surface termination and stacking faults in the PBA prepared Co_2C may result in better overall performance.[70,71] Although the initial OER activities of the nanocarbides are low compared to state-of-the-art electrocatalysts such as IrO_2 and RuO_2,[3,72,73] the robust electrochemical stability in harsh alkaline conditions shows promise for long-term activity.[74,75]

Electrochemical Activity Toward HER. HER activity was assessed using linear sweep voltammograms (LSVs) in acidic conditions, as shown in Figure 5a,f. HER activity in alkaline

https://doi.org/10.1021/acs.inorgchem.2c01713
Inorg. Chem. 2022, 61, 13836–13845

conditions is available in Supporting Information Figure S23 and is observed to be < −0.6 V. HER activity for Fe_3C in acidic conditions is consistent with the reported HER activity for Fe_5C_2.[16,76] HER activity for Co_2C does not reach 10 mA. In acidic conditions, Ni_3C carbide was the only carbide to exhibit significant HER activity with an overpotential of −0.412 V, which indicates that Ni_3C has potential as a bifunctional HER/OER electrocatalyst. The Tafel slope for Ni_3C in these conditions was 170 mV dec^{-1}, close to the theoretical value reported for the Volmer step being rate-limiting for HER (120 mV dec^{-1}), indicating slow kinetics for hydrogen adsorption.[77,78] The Ni_3C Tafel slope data are available in Supporting Information Figure S24. Comparison of the performance in HER is compared to reported Fe, Ni, and Co M-xides in Supporting Information Table S6.

CONCLUSIONS

Developing sustainable and scalable routes to first row TM catalysts that can replace platinum group elements is a critical target in water-splitting devices, fuel cells, and CO_2 reduction to name a few. Metal carbides are of interest because of high natural abundance, increased stability, and improved perfomance.[4] We developed a solvothermal route to convert a single-source coordination polymer into targeted nanometal carbides. The nanocarbides are single-phase, have a spherical geometry, and 20−25% RMS size distributions.

The observation of OER and HER activity in the TM-carbides formed using PBA templating methods is promising. A comparison of the measured values for PBA-grown Fe, Co, and Ni carbides to the literature values of reported OER and HER catalysts is provided in the Supporting information (SI Tables S5 and S6). The measured overpotentials for OER and HER of the PBA prepared Fe, Co, and Ni carbides are consistent with previous reports for Ni_3C,[24] Fe:Ni_3C,[24] and Co:Ni_3C[10] formed from Ni-PBA through furnace methods. Of the catalysts, only the Ni_3C is an amphoteric electrocatalyst for water-splitting reactions. While the Ni_3C does not perform as well in comparison to the established literature, it is suggested that the size, morphology, and nitrogen-doped graphene supports may be influencing factors for better electrocatalytic activity.[9] It is worth noting, however, that a report on bimetallic carbides observed enhancement of HER in Fe:Ni_3C, suggesting further studies into bimetallic carbides prepared using bimetallic PBAs for enhanced reactivity may be of benefit due to synergistic effects previously reported in the literature.[24,79−85] Further studies are underway to explore bimetallic carbides to improve the bifunctional performance of binary carbides prepared from binary PBA single-source precursors.

The ability to scale the PBA to carbide conversion synthesis using commercial sources, as well as the wealth of PBAs known in the literature, offers great potential. The ability to systematically prepare binary, ternary, or quaternary carbides using this method is potentially important as the mixed metal carbides are better catalysts than the single component carbides.[10,24,86] When coupled to the fact that synthesis of PBA precursors in water is sustainable and the carbide formation is facile, it is reasonable to expect that a wide range of carbide-based catalysts could be formed and studies using the developed PBA to carbide route are underway for a wide range of catalysts systems, including electrocatalytic water splitting, CO_2 reduction, and Fischer−Tropsch process.

EXPERIMENTAL SECTION

Iron Prussian blue was commercially sourced (Acros Organics). The PBAs were prepared using commercial reagents potassium hexacyanocobaltate(III) ($K_3Co(CN)_6$, Sigma-Aldrich, >97.0%), potassium tetracyanonickelate(II) hydrate (Alfa Aesar), cobalt(II) chloride hexahydrate ($CoCl_2{\cdot}6H_2O$, Alfa Aesar 99.9%), nickel(II) chloride hexahydrate (Fisher Scientific, > 99%), and potassium chloride (Sigma, 98%). Solvents used in the synthesis were nanopure water (Barnstead NANOpure), methanol (BDH, ACS grade), toluene (Macron, ACS grade), acetone (Macron, ACS Grade), octadecylamine (Acros, 90%), Nafion (BeanTown Chemical), 1 M potassium hydroxide (Millipore Sigma). Biobeads sx-2 resin (Bio-Rad). **Caution!** Transition metal cyanides may produce HCN in the presence of acid or if heated as a dry powder.

Synthesis of a M-PBA ($K[CoCo(CN)_6]{\cdot}xH_2O$; $Ni[Ni(CN)_4]$). M-PBAs were prepared following literature precedence procedure using a coprecipitation reaction at room temperature.[43] Briefly, the Co-PBA is synthesized by coprecipitation at room temperature. Aqueous 20 mM $K_3Co(CN)_6$ solution (50 mL) and 50 mL of aqueous 0.1 M KCl were mixed together for 10 min. Aqueous 5 mM $CoCl_2{\cdot}6H_2O$ (200 mL) was added dropwise at a rate of 5 mL/min. Upon completion of the injection, the reaction was matured for 18 h, and the resulting product was isolated via acetone-assisted centrifugation. Particles were then resuspended in acetone and allowed to dry overnight.

The Ni-PBA is synthesized using a coprecipitation method at room temperature. The aqueous 20 mM $K_2Ni(CN)_4$ solution (50 mL) and 50 mL of aqueous 0.1 M KCl were mixed together for 10 min. Aqueous 5 mM $NiCl_2{\cdot}6H_2O$ (200 mL) was added dropwise at a rate of 5 mL/min. Upon completion of the injection, the reaction was matured for 18 h, and the resulting product was isolated via acetone-assisted centrifugation. Particles were then resuspended in acetone and allowed to dry overnight.

Thermal Conversion of a M-PBA to M_xC. The conversion of M-PBA (M = Fe, Co, Ni) to M_xC was carried out in 4 mL of octadecylamine containing 0.04 g of M-PBA. Scaleup reactions were accomplished using the same procedure by 0.05 g, 0.25, 2.5 g of Fe-PB in 10 g, 30 g, 300 g of octadecylamine, respectively.

The solution was heated to 50 °C under vacuum for 1 h to remove O_2. The reaction vessel was charged with N_2, heated at reflux (350 °C at a rate of 20 °C /min) for 1 h, and rapidly cooled to room temperature by forced air. The nanocarbides were precipitated by the addition of 3:1 v:v toluene−methanol as a cosolvent, isolated via centrifugation, and washed three times with toluene and methanol (3:1 v:v). The particles were dried overnight by vacuum and stored under N_2 (g).

Caution! Transition metal cyanides may produce HCN in the presence of acid or if heated as dry powder. Prussian blue and its analogues can produce free cyanide when heated. Although no evidence of free cyanide is observed in the solution following solvothermal conversion of the PB and PBA to metal carbide (as tested below), all experiments should be performed in a properly ventilated reaction environment to reduce risk of exposure to free cyanide.

Testing for Free Cyanide. The solution following conversion to the M_xC was tested for free cyanide using a cyanide testing kit (Quantofix Cyanid, Macherey-Nagel). The isolated nanocrystals were sonicated in nanopure H_2O to solvate the potential anion and mixed with two proprietary buffer solutions. The resulting liquid was dropped onto a colormetric test strip and rested for 30 s before the test strip was compared to a cyanide concentration chart. No free cyanide was detected in the solution.

Physical Measurements. X-ray powder patterns were collected at room temperature on a Rigaku Miniflex powder diffractometer (Cu Kα source). pXRD measurements on XPS sputtered samples were performed on a Rigaku Synergy single crystal diffractometer running in powder diffraction mode (Mo Kα).

X-ray photoelectron spectroscopy (XPS) was performed on M_xC powders deposited on carbon tape using a PHI 5100 X-ray photoelectron spectrometer. XPS has an excitation source of Mg

https://doi.org/10.1021/acs.inorgchem.2c01713
Inorg. Chem. 2022, 61, 13836−13845

Kα, with a pass energy of 22.36 eV to minimize linewidth. Samples were Ar^+-sputtered with a puck rotation of two revolutions per minute using a sputtering gun at 5 keV and 1 μA for five minutes. All samples were calibrated to the aliphatic carbon assignment (C1s 284.8 eV).

Size, size dispersity, morphology, and lattice fringe analysis were conducted by TEM. TEM images were collected on a Tecnai Osiris TEM/STEM operating at 200 kV. High-resolution microstructure characterization was performed using an aberration-corrected JEOL ARM 200 F TEM operated at 200 kV. The M_xC sample for TEM was prepared by dispersing the M_xC in toluene and octadecylamine (10:1 v:v), heated in an oil bath at 50 °C for 12 h, sonicated in a heated bath for 2 min, and ran through a gel permeation chromatography column to remove excess ligand and aggregated solid.[51] The solution was drop-cast onto a carbon-coated 200 mesh gold TEM grids (Ted Pella 01840G), excess solvent wicked away with a Kimwipe 2 s after deposition, and dried in a vacuum oven at 80 °C for 12 h.

Electrochemical Setup and Measurements. Pure-phase Fe_3C, Co_2C, and Ni_3C nanoparticles (0.7 mg mL^{-1}) were prepared in a suspension of 10% Nafion solution (5% (w/w) in water/1-propanol, 6% ethanol, and 84% nanopure water. Nanoparticle suspensions were sonicated for 2−5 min until well-dispersed. The suspension was drop-cast onto a 5 mm diameter PTFE-embedded glassy carbon (GC) rotating disk electrode (RDE) (Pine Research Instrumentation) that had been polished in 0.05 μm alumina suspension on a microcloth polishing pad (Buehler) for 1 min, followed by di H_2O on a microcloth polishing pad for 1 min. The drop-casted nanoparticle suspension dried as a homogenous, thin-layer film on the GCE surface at room temperature for 1−2 h, with each sample having a consistent mass loading of nanoparticles of 0.1 mg cm^{-2}. Electrochemical measurements were performed in an electrochemical glass cell (Pine Research Instrumentation) using a three-electrode set up with a GC working electrode, a Ag/AgCl reference electrode, and a graphite rod counter electrode. The working electrode was rotated at 1500 rpm using a PINE rotator (WaveVortex 10, Pine Research Instrumentation) connected to a potentiostat (model CH 660E, CH Instruments). The ECSA of each sample was estimated from electrochemical double layer capacitance (C_{dl}) using CV in a potential window of 0.8−0.95 V vs RHE with chosen scan rates of 10, 20, 50, and 100 mV s^{-1}. The ECSA was calculated using the extracted value of C_{dl} and the specific capacitance (C_s) of glassy carbon from the literature (45 μF cm^{-2})[87,88] using ECSA = C_{dl}/C_s. Electrochemical OER measurements were performed in alkaline conditions in 1 M KOH electrolyte using a potential range of 1.0−1.8 V vs the reversible hydrogen electrode (RHE), using CV with a scan rate of 10 mV s^{-1}. Preliminary electrochemical HER measurements were assessed in acidic conditions using 0.5 M H_2SO_4 electrolyte within a potential range of 0.0 to −0.6 V vs RHE and alkaline conditions within a potential range of 0.0 to −0.8 V. The stability of electroactivity toward the OER was monitored using repetitive CVs (n = 100), in 1.0 M KOH between 1.0 and 1.8 V vs RHE, for a 4.5 h duration. Samples prepared for post-OER analysis were dropcasted onto a glassy carbon wafer with an estimated mass loading of 0.8 mg cm^{-2} and ran for 20 CV cycles. The potentials in this work were converted from being against the Ag/AgCl reference electrode to the RHE using $E_{vs.}$ RHE = $E_{vsAg/AgCl}$ + 0.059(pH) + $E^{\circ}_{vsAg/AgCl}$. Additionally, the reference used experimentally was always within 5 mV difference of a master Ag/AgCl reference, not used in experiments. The overpotential (η) for the OER was determined using $\eta = E_{vs.\ RHE} - 1.23$ V. The overpotential at a current density of 10 mA cm^{-2}, normalized to the geometry and ECSA, was extracted from each voltammogram and rounded to the nearest 10 mV.

■ ASSOCIATED CONTENT

Supporting Information

The Supporting Information is available free of charge at https://pubs.acs.org/doi/10.1021/acs.inorgchem.2c01713.

Video of bubbles coming off a Co_2C-nafion medium drop-casted on a glassy carbon electrode for OER activity measurements (MPG)

Histograms of the TEM images of the M_xC nanoparticles; SEM images and histograms of the M-PBA precursor; dark field images of the Co_2C with fringe analysis showing spinel terminations; complete annotations of the HRTEM images of the Fe_3C and Co_2C strained particles; HRTEM of the Ni_3C nanoparticles; Raman spectra showing an absence of the d/g bands for each of the M_xC nanocrystals; TEM illustrating nanocrystal changes in Fe_3C and Ni_3C as a function of time; carbon growth on a Fe_3C nanocrystal as a function of time; XPS surveys of the as-synthesized and post OER samples, pre and post sputtered; tables with the peak position and FWHM of the pre- and postsputtered M_xC samples; image of free cyanide testing on Fe_3C; Tafel analysis of the M_xC for OER and HER; HER activity of M_xC in alkaline conditions; and table of existing Fe, Co, and Ni MXides and their sample preparation, reaction conditions, and measured overpotentials (PDF)

■ AUTHOR INFORMATION

Corresponding Author

Geoffrey F. Strouse − *Department of Chemistry and Biochemistry, Florida State University, Tallahassee, Florida 32306, United States;* orcid.org/0000-0003-0841-282X; Email: gstrouse@fsu.edu

Authors

Edward T. Nguyen − *Department of Chemistry and Biochemistry, Florida State University, Tallahassee, Florida 32306, United States;* orcid.org/0000-0002-4787-8270

Isabella A. Bertini − *Department of Chemistry and Biochemistry, Florida State University, Tallahassee, Florida 32306, United States;* orcid.org/0000-0001-8365-7259

Amanda J. Ritz − *Department of Chemistry and Biochemistry, Florida State University, Tallahassee, Florida 32306, United States;* orcid.org/0000-0003-2767-9079

Robert A. Lazenby − *Department of Chemistry and Biochemistry, Florida State University, Tallahassee, Florida 32306, United States;* orcid.org/0000-0002-3622-4108

Keyou Mao − *Department of Industrial and Manufacturing Engineering, FAMU-FSU College of Engineering, Tallahassee, Florida 32310, United States; National High Magnetic Field Laboratory, Tallahassee, Florida 32310, United States;* orcid.org/0000-0002-2909-8131

James R. McBride − *Vanderbilt Institute of Nanoscale Science and Engineering, Nashville, Tennessee 37235, United States;* orcid.org/0000-0003-0161-7283

Alexzandra V. Mattia − *Department of Chemistry and Biochemistry, Florida State University, Tallahassee, Florida 32306, United States*

Jason E. Kuszynski − *Department of Chemistry and Biochemistry, Florida State University, Tallahassee, Florida 32306, United States;* orcid.org/0000-0002-9458-6940

Samuel F. Wenzel − *Department of Chemistry and Biochemistry, Florida State University, Tallahassee, Florida 32306, United States;* orcid.org/0000-0003-3314-4521

Sarah D. Bennett − *Department of Chemistry and Biochemistry, Florida State University, Tallahassee, Florida 32306, United States;* orcid.org/0000-0001-8124-1049

Complete contact information is available at: https://pubs.acs.org/10.1021/acs.inorgchem.2c01713

https://doi.org/10.1021/acs.inorgchem.2c01713
Inorg. Chem. 2022, 61, 13836−13845

Author Contributions

Synthesis of the PBA precursor and conversion was performed by E.T.N., I.A.B., S.D.B., and A.V.M. Electrocatalytic experiments were designed and conducted by A.J.R., S.F.W. and R.A.L. TEM experiments were conducted by R.A.L. and K.M. All characterization was done by E.T.N., I.A.B., A.J.R., R.A.L., K.M., and J.E.K. Interpretation of the data and intellectual discussions were conducted by E.T.N., I.A.B., A.J.R., R.A.L., K.M., J.R.M., J.E.K., and G.F.S. The manuscript was prepared by E.T.N., I.A.B., A.J.R., R.A.L., and G.F.S. All authors have given approval to the final version of the manuscript.

Notes

The authors declare no competing financial interest.

■ ACKNOWLEDGMENTS

GFS wishes to thank the National Science Foundation (NSF) (CHE-1608364) "SusChEM: Understanding Microwave Interactions to Control Magnetic Nanocrystal Growth from a Single Source Precursor" for funding. R.A.L. gratefully acknowledges Florida State University for funding. We thank the Hanson lab at FSU for supplying the notch filter for Raman spectroscopy. We would like to thank Xinsong Lin and Eric J Lochner for intellectual contributions to the electron microscopy, crystallography, and XPS interpretation, respectively. A portion of the TEM work was performed by Dr. Yan Xin at the National High Magnetic Field Laboratory, which is supported by National Science Foundation Cooperative Agreement No. DMR-1644779, and the State of Florida. A portion of the work was conducted in the FSU Department of Chemistry & Biochemistry's MAC (FSU075000MAC) and X-ray (FSU075000XRAY) Laboratories.

■ REFERENCES

(1) Zhang, C.; Tang, D.; Hu, X.; Liu, X.; Zhang, T.; Zhou, H. Scalable synthesis and excellent catalytic effect of hydrangea-like RuO2 mesoporous materials for lithium−O2 batteries. *Energy Storage Mater.* **2016**, *2*, 8−13.

(2) Kong, C.; Min, S.; Lu, G. Robust Pt−Sn alloy decorated graphene nanohybrid cocatalyst for photocatalytic hydrogen evolution. *Chem. Commun.* **2014**, *50*, 9281−9283.

(3) McCrory, C. C. L.; Jung, S.; Ferrer, I. M.; Chatman, S. M.; Peters, J. C.; Jaramillo, T. F. Benchmarking Hydrogen Evolving Reaction and Oxygen Evolving Reaction Electrocatalysts for Solar Water Splitting Devices. *J. Am. Chem. Soc.* **2015**, *137*, 4347−4357.

(4) Wygant, B. R.; Kawashima, K.; Mullins, C. B. Catalyst or Precatalyst? The Effect of Oxidation on Transition Metal Carbide, Pnictide, and Chalcogenide Oxygen Evolution Catalysts. *ACS Energy Lett.* **2018**, *3*, 2956−2966.

(5) Wang, Y.; Wu, Q.; Zhang, B.; Tian, L.; Li, K.; Zhang, X. Recent Advances in Transition Metal Carbide Electrocatalysts for Oxygen Evolution Reaction. *Catalysts* **2020**, *10*, 1164.

(6) Qie, Y.; Liu, Y.; Kong, F.; Yang, Z.; Yang, H. High coercivity cobalt carbide nanoparticles as electrocatalysts for hydrogen evolution reaction. *Nano Res.* **2022**, *15*, 3901.

(7) Joo, S. H.; Lee, J. S. Metal carbides as alternative electrocatalysts for energy conversion reactions. *J. Catal.* **2021**, *404*, 911−924.

(8) Ede, S. R.; Luo, Z. Tuning the intrinsic catalytic activities of oxygen-evolution catalysts by doping: a comprehensive review. *J. Mater. Chem. A* **2021**, *9*, 20131−20163.

(9) Jin, J.; Yin, J.; Liu, H.; Lu, M.; Li, J.; Tian, M.; Xi, P. Transition Metal (Fe, Co and Ni)−Carbide−Nitride (M−C−N) Nanocatalysts: Structure and Electrocatalytic Applications. *ChemCatChem* **2019**, *11*, 2780−2792.

(10) Jia, X.; Wang, M.; Liu, G.; Wang, Y.; Yang, J.; Li, J. Mixed-metal MOF-derived Co-doped Ni3C/Ni NPs embedded in carbon matrix as an efficient electrocatalyst for oxygen evolution reaction. *Int. J. Hydrogen Energy* **2019**, *44*, 24572−24579.

(11) Xiao, Y.; Sun, P.; Cao, M. Core−Shell Bimetallic Carbide Nanoparticles Confined in a Three-Dimensional N-Doped Carbon Conductive Network for Efficient Lithium Storage. *ACS Nano* **2014**, *8*, 7846−7857.

(12) Wu, H. B.; Xia, B. Y.; Yu, L.; Yu, X.-Y.; Lou, X. W. Porous molybdenum carbide nano-octahedrons synthesized via confined carburization in metal-organic frameworks for efficient hydrogen production. *Nat. Commun.* **2015**, *6*, 6512.

(13) Schmuecker, S. M.; Clouser, D.; Kraus, T. J.; Leonard, B. M. Synthesis of metastable chromium carbide nanomaterials and their electrocatalytic activity for the hydrogen evolution reaction. *Dalton Trans.* **2017**, *46*, 13524−13530.

(14) Li, S.; Yang, C.; Yin, Z.; Yang, H.; Chen, Y.; Lin, L.; Li, M.; Li, W.; Hu, G.; Ma, D. Wet-chemistry synthesis of cobalt carbide nanoparticles as highly active and stable electrocatalyst for hydrogen evolution reaction. *Nano Res.* **2017**, *10*, 1322−1328.

(15) Ma, R.; Song, E.; Zhou, Y.; Zhou, Z.; Liu, G.; Liu, Q.; Liu, J.; Zhu, Y.; Wang, J. Ultrafine WC nanoparticles anchored on co-encased, N-doped carbon nanotubes for efficient hydrogen evolution. *Energy Storage Mater.* **2017**, *6*, 104−111.

(16) Li, S.; Yang, J.; Song, C.; Zhu, Q.; Xiao, D.; Ma, D. Iron Carbides: Control Synthesis and Catalytic Applications in COx Hydrogenation and Electrochemical HER. *Adv. Mater.* **2019**, *31*, No. 1901796.

(17) Li, Z.; Fu, J.-Y.; Feng, Y.; Dong, C.-K.; Liu, H.; Du, X.-W. A silver catalyst activated by stacking faults for the hydrogen evolution reaction. *Nat. Catal.* **2019**, *2*, 1107−1114.

(18) Xu, Y.; Zhang, F.; Sheng, T.; Ye, T.; Yi, D.; Yang, Y.; Liu, S.; Wang, X.; Yao, J. Clarifying the controversial catalytic active sites of Co3O4 for the oxygen evolution reaction. *J. Mater. Chem. A* **2019**, *7*, 23191−23198.

(19) Plummer, L. K.; Hutchison, J. E. Understanding the Effects of Iron Precursor Ligation and Oxidation State Leads to Improved Synthetic Control for Spinel Iron Oxide Nanocrystals. *Inorg. Chem.* **2020**, *59*, 15074−15087.

(20) Kim, J.-H.; Kawashima, K.; Wygant, B. R.; Mabayoje, O.; Liu, Y.; Wang, J. H.; Mullins, C. B. Transformation of a Cobalt Carbide (Co3C) Oxygen Evolution Precatalyst. *ACS Appl. Energy Mater.* **2018**, *1*, 5145−5150.

(21) Eckstrom, H. C.; Adcock, W. A. A New Iron Carbide In Hydrocarbon Synthesis Catalysts. *J. Am. Chem. Soc.* **1950**, *72*, 1042−1043.

(22) Goto, Y.; Taniguchi, K.; Omata, T.; Otsuka-Yao-Matsuo, S.; Ohashi, N.; Ueda, S.; Yoshikawa, H.; Yamashita, Y.; Oohashi, H.; Kobayashi, K. Formation of Ni3C Nanocrystals by Thermolysis of Nickel Acetylacetonate in Oleylamine: Characterization Using Hard X-ray Photoelectron Spectroscopy. *Chem. Mater.* **2008**, *20*, 4156−4160.

(23) Wang, H.; Cao, Y.; Zou, G.; Yi, Q.; Guo, J.; Gao, L. High-Performance Hydrogen Evolution Electrocatalyst Derived from Ni3C Nanoparticles Embedded in a Porous Carbon Network. *ACS Appl. Mater. Interfaces* **2017**, *9*, 60−64.

(24) Fan, H.; Yu, H.; Zhang, Y.; Zheng, Y.; Luo, Y.; Dai, Z.; Li, B.; Zong, Y.; Yan, Q. Fe-Doped Ni3C Nanodots in N-Doped Carbon Nanosheets for Efficient Hydrogen-Evolution and Oxygen-Evolution Electrocatalysis. *Angew. Chem. Int. Ed.* **2017**, *56*, 12566−12570.

(25) Gong, Q.; Wang, Y.; Hu, Q.; Zhou, J.; Feng, R.; Duchesne, P. N.; Zhang, P.; Chen, F.; Han, N.; Li, Y.; Jin, C.; Li, Y.; Lee, S.-T. Ultrasmall and phase-pure W2C nanoparticles for efficient electrocatalytic and photoelectrochemical hydrogen evolution. *Nat. Commun.* **2016**, *7*, 13216.

(26) Politi, J. R.; Viñes, F.; Rodriguez, J. A.; Illas, F. Atomic and electronic structure of molybdenum carbide phases: bulk and low Miller-index surfaces. *Phys. Chem. Chem. Phys.* **2013**, *15*, 12617−12625.

(27) Yang, C.; Zhao, H.; Hou, Y.; Ma, D. Fe5C2 Nanoparticles: A Facile Bromide-Induced Synthesis and as an Active Phase for

https://doi.org/10.1021/acs.inorgchem.2c01713
Inorg. Chem. 2022, 61, 13836−13845

Fischer−Tropsch Synthesis. *J. Am. Chem. Soc.* **2012**, *134*, 15814−15821.
(28) Carroll, K. J.; Huba, Z. J.; Spurgeon, S. R.; Qian, M.; Khanna, S. N.; Hudgins, D. M.; Taheri, M. L.; Carpenter, E. E. Magnetic properties of Co2C and Co3C nanoparticles and their assemblies. *Appl. Phys. Lett.* **2012**, *101*, No. 012409.
(29) Zhang, Y.; Zhu, Y.; Wang, K.; Li, D.; Wang, D.; Ding, F.; Meng, D.; Wang, X.; Choi, C.; Zhang, Z. Controlled synthesis of Co2C nanochains using cobalt laurate as precursor: Structure, growth mechanism and magnetic properties. *J. Magn. Magn. Mater.* **2018**, *456*, 71−77.
(30) Nagai, M.; Matsuda, K. Low-temperature water−gas shift reaction over cobalt−molybdenum carbide catalyst. *J. Catal.* **2006**, *238*, 489−496.
(31) Silva, C. G.; Passos, F. B.; Teixeira da Silva, V. Effect of Carburization Conditions on the Activity of Molybdenum Carbide-Supported Catalysts Promoted by Nickel for the Dry Reforming of Methane. *Energy Fuels* **2021**, *35*, 17833−17847.
(32) Cumberland, S. L.; Hanif, K. M.; Javier, A.; Khitrov, G. A.; Strouse, G. F.; Woessner, S. M.; Yun, C. S. Inorganic Clusters as Single-Source Precursors for Preparation of CdSe, ZnSe, and CdSe/ZnS Nanomaterials. *Chem. Mater.* **2002**, *14*, 1576−1584.
(33) Gary, D. C.; Terban, M. W.; Billinge, S. J. L.; Cossairt, B. M. Two-Step Nucleation and Growth of InP Quantum Dots via Magic-Sized Cluster Intermediates. *Chem. Mater.* **2015**, *27*, 1432−1441.
(34) Fletcher, D. C.; Hunter, R.; Xia, W.; Smales, G. J.; Pauw, B. R.; Blackburn, E.; Kulak, A.; Xin, H.; Schnepp, Z. Scalable synthesis of dispersible iron carbide (Fe3C) nanoparticles by 'nanocasting'. *J. Mater. Chem. A* **2019**, *7*, 19506−19512.
(35) Oar-Arteta, L.; Wezendonk, T.; Sun, X.; Kapteijn, F.; Gascon, J. Metal organic frameworks as precursors for the manufacture of advanced catalytic materials. *Mater. Chem. Front.* **2017**, *1*, 1709−1745.
(36) Wang, X.; Dong, A.; Zhu, Z.; Chai, L.; Ding, J.; Zhong, L.; Li, T.-T.; Hu, Y.; Qian, J.; Huang, S. Surfactant-Mediated Morphological Evolution of MnCo Prussian Blue Structures. *Small* **2020**, *16*, No. 2004614.
(37) de Smit, E.; Cinquini, F.; Beale, A. M.; Safonova, O. V.; van Beek, W.; Sautet, P.; Weckhuysen, B. M. Stability and Reactivity of $\epsilon-\chi-\theta$ Iron Carbide Catalyst Phases in Fischer−Tropsch Synthesis: Controlling μC. *J. Am. Chem. Soc.* **2010**, *132*, 14928−14941.
(38) Yamada, M.; Arai, M.; Kurihara, M.; Sakamoto, M.; Miyake, M. Synthesis and Isolation of Cobalt Hexacyanoferrate/Chromate Metal Coordination Nanopolymers Stabilized by Alkylamino Ligand with Metal Elemental Control. *J. Am. Chem. Soc.* **2004**, *126*, 9482−9483.
(39) Yamada, M.; Okumura, S.-j.; Takahashi, K. Synthesis and Film Formation of Magnetic FeCo Nanoparticles with Graphitic Carbon Shells. *J. Phys. Chem. Lett.* **2010**, *1*, 2042−2045.
(40) Burshtein, T. Y.; Aias, D.; Wang, J.; Sananis, M.; Farber, E. M.; Gazit, O. M.; Grinberg, I.; Eisenberg, D. Fe−N−C electrocatalysts in the oxygen and nitrogen cycles in alkaline media: the role of iron carbide. *Phys. Chem. Chem. Phys.* **2021**, *23*, 26674−26679.
(41) Li, B.; Liu, G.; Yang, S.; Wang, H.; Li, J.; Wu, J. FeCx@C catalysts prepared from Prussian blue and their applications in Fischer-Tropsch synthesis. *Appl. Catal., A* **2022**, *638*, No. 118609.
(42) Wang, Q.; Shi, S.; Wu, F.; Zhang, Z.; Li, G.; Zheng, Y.; Suo, Y. Bimetallic CoZn Nanocrystals Embedded in N-Doped Graphene Layers as Electrocatalysts for Oxygen Reduction Reaction. *Catal. Lett.* **2022**, *152*, 1950.
(43) Hardy, D. A.; Nguyen, E. T.; Parrish, S. E.; Schriber, E. A.; Schlicker, L.; Gili, A.; Kamutzki, F.; Hohman, J. N.; Strouse, G. F. Prussian Blue Iron−Cobalt Mesocrystals as a Template for the Growth of Fe/Co Carbide (Cementite) and Fe/Co Nanocrystals. *Chem. Mater.* **2019**, *31*, 8163−8173.
(44) Aparicio, C.; Machala, L.; Marusak, Z. Thermal decomposition of Prussian blue under inert atmosphere. *J. Therm. Anal. Calorim.* **2012**, *110*, 661−669.
(45) Regmi, Y. N.; Leonard, B. M. General Synthesis Method for Bimetallic Carbides of Group VIIIA First Row Transition Metals with Molybdenum and Tungsten. *Chem. Mater.* **2014**, *26*, 2609−2616.
(46) Gao, S.; Chen, H.; Liu, Y.; Li, G.-D.; Gao, R.; Zou, X. Surface-clean, phase-pure multi-metallic carbides for efficient electrocatalytic hydrogen evolution reaction. *Inorg. Chem. Front.* **2019**, *6*, 940−947.
(47) Zakaria, M. B.; Chikyow, T. Recent advances in Prussian blue and Prussian blue analogues: synthesis and thermal treatments. *Coord. Chem. Rev.* **2017**, *352*, 328−345.
(48) Bhadeshia, H. K. D. H.; Honeycombe, S. R. The Effects of Alloying Elements on Iron-Carbon Alloys. In *Steels*, 3rd edition; Bhadeshia, H. K. D. H., Honeycombe, S. R., Eds.; Butterworth-Heinemann, 2006; pp. 71−93.
(49) Zhang, T.; Wu, J.; Xu, Y.; Wang, X.; Ni, J.; Li, Y.; Niemantsverdriet, J. W. Cobalt and cobalt carbide on alumina/NiAl(110) as model catalysts. *Catal. Sci. Technol.* **2017**, *7*, 5893−5899.
(50) Esmaeilirad, M.; Baskin, A.; Kondori, A.; Sanz-Matias, A.; Qian, J.; Song, B.; Tamadoni Saray, M.; Kucuk, K.; Belmonte, A. R.; Delgado, P. N. M.; Park, J.; Azari, R.; Segre, C. U.; Shahbazian-Yassar, R.; Prendergast, D.; Asadi, M. Gold-like activity copper-like selectivity of heteroatomic transition metal carbides for electrocatalytic carbon dioxide reduction reaction. *Nat. Commun.* **2021**, *12*, 5067.
(51) Shen, Y.; Roberge, A.; Tan, R.; Gee, M. Y.; Gary, D. C.; Huang, Y.; Blom, D. A.; Benicewicz, B. C.; Cossairt, B. M.; Greytak, A. B. Gel permeation chromatography as a multifunctional processor for nanocrystal purification and on-column ligand exchange chemistry. *Chem. Sci.* **2016**, *7*, 5671−5679.
(52) Li, B. Q.; Sui, M. L.; Mao, S. X. Pseudoelastic stacking fault and deformation twinning in nanocrystalline Ni. *Appl. Phys. Lett.* **2010**, *97*, 241912.
(53) Wang, L.; Du, K.; Yang, C.; Teng, J.; Fu, L.; Guo, Y.; Zhang, Z.; Han, X. In situ atomic-scale observation of grain size and twin thickness effect limit in twin-structural nanocrystalline platinum. *Nat. Commun.* **2020**, *11*, 1167.
(54) Hu, X.; Björkman, T.; Lipsanen, H.; Sun, L.; Krasheninnikov, A. V. Solubility of Boron, Carbon, and Nitrogen in Transition Metals: Getting Insight into Trends from First-Principles Calculations. *J. Phys. Chem. Lett.* **2015**, *6*, 3263−3268.
(55) Gili, A.; Schlicker, L.; Bekheet, M. F.; Görke, O.; Penner, S.; Grünbacher, M.; Götsch, T.; Littlewood, P.; Marks, T. J.; Stair, P. C.; Schomäcker, R.; Doran, A.; Selve, S.; Simon, U.; Gurlo, A. Surface Carbon as a Reactive Intermediate in Dry Reforming of Methane to Syngas on a 5% Ni/MnO Catalyst. *ACS Catal.* **2018**, *8*, 8739−8750.
(56) Yoshida, H.; Takeda, S.; Uchiyama, T.; Kohno, H.; Homma, Y. Atomic-Scale In-situ Observation of Carbon Nanotube Growth from Solid State Iron Carbide Nanoparticles. *Nano Lett.* **2008**, *8*, 2082−2086.
(57) Glaser, F. W.; Ivanick, W. Sintered Titanium Carbide. *JOM* **1952**, *4*, 387−390.
(58) Koc, R.; Kodambaka, S. K. Tungsten carbide (WC) synthesis from novel precursors. *J. Eur. Ceram. Soc.* **2000**, *20*, 1859−1869.
(59) Hwu, H. H.; Chen, J. G. Surface Chemistry of Transition Metal Carbides. *Chem. Rev.* **2005**, *105*, 185−212.
(60) Xiao, Y.; Hwang, J.-Y.; Sun, Y.-K. Transition metal carbide-based materials: synthesis and applications in electrochemical energy storage. *J. Mater. Chem. A* **2016**, *4*, 10379−10393.
(61) Engstrand, T. O.; Cope, E. M.; Vasquez, G.; Haddock, J. W.; Hertz, M. B.; Wang, X.; Latturner, S. E. Flux Synthesis of a Metal Carbide Hydride Using Anthracene As a Reactant. *Inorg. Chem.* **2020**, *59*, 11651−11657.
(62) Wakisaka, T.; Kusada, K.; Wu, D.; Yamamoto, T.; Toriyama, T.; Matsumura, S.; Akiba, H.; Yamamuro, O.; Ikeda, K.; Otomo, T.; Palina, N.; Chen, Y.; Kumara, L. S. R.; Song, C.; Sakata, O.; Xie, W.; Koyama, M.; Kubota, Y.; Kawaguchi, S.; Arevalo, R. L.; Aspera, S. M.; Arguelles, E. F.; Nakanishi, H.; Kitagawa, H. Rational Synthesis for a Noble Metal Carbide. *J. Am. Chem. Soc.* **2020**, *142*, 1247−1253.
(63) Cabrera-German, D.; Gomez-Sosa, G.; Herrera-Gomez, A. Accurate peak fitting and subsequent quantitative composition analysis of the spectrum of Co 2p obtained with Al Kα radiation: I: cobalt spinel. *Surf. Interface Anal.* **2016**, *48*, 252−256.

https://doi.org/10.1021/acs.inorgchem.2c01713
Inorg. Chem. 2022, 61, 13836−13845

(64) Zhu, C.; Wang, A.-L.; Xiao, W.; Chao, D.; Zhang, X.; Tiep, N. H.; Chen, S.; Kang, J.; Wang, X.; Ding, J.; Wang, J.; Zhang, H.; Fan, H. J. In Situ Grown Epitaxial Heterojunction Exhibits High-Performance Electrocatalytic Water Splitting. *Adv. Mater.* **2018**, *30*, No. 1705516.
(65) Hou, L.; Liang, Q.; Wang, F. Mechanisms that control the adsorption−desorption behavior of phosphate on magnetite nanoparticles: the role of particle size and surface chemistry characteristics. *RSC Adv.* **2020**, *10*, 2378−2388.
(66) Yang, J.; Cheng, H.; Frost, R. L. Synthesis and characterisation of cobalt hydroxy carbonate Co2CO3(OH)2 nanomaterials. *Spectrochim. Acta, Part A* **2011**, *78*, 420−428.
(67) Yang, C. C.; Zai, S. F.; Zhou, Y. T.; Du, L.; Jiang, Q. Fe3C-Co Nanoparticles Encapsulated in a Hierarchical Structure of N-Doped Carbon as a Multifunctional Electrocatalyst for ORR, OER, and HER. *Adv. Funct. Mater.* **2019**, *29*, No. 1901949.
(68) Anantharaj, S.; Ede, S. R.; Karthick, K.; Sam Sankar, S.; Sangeetha, K.; Karthik, P. E.; Kundu, S. Precision and correctness in the evaluation of electrocatalytic water splitting: revisiting activity parameters with a critical assessment. *Energy Environ. Sci.* **2018**, *11*, 744−771.
(69) Rountree, E. S.; McCarthy, B. D.; Eisenhart, T. T.; Dempsey, J. L. Evaluation of Homogeneous Electrocatalysts by Cyclic Voltammetry. *Inorg. Chem.* **2014**, *53*, 9983−10002.
(70) Wan, C.; Leonard, B. M. Iron-Doped Molybdenum Carbide Catalyst with High Activity and Stability for the Hydrogen Evolution Reaction. *Chem. Mater.* **2015**, *27*, 4281−4288.
(71) Yang, C.; Zhao, R.; Xiang, H.; Wu, J.; Zhong, W.; Li, W.; Zhang, Q.; Yang, N.; Li, X. Ni-Activated Transition Metal Carbides for Efficient Hydrogen Evolution in Acidic and Alkaline Solutions. *Adv. Energy Mater.* **2020**, *10*, No. 2002260.
(72) Jung, S.; McCrory, C. C. L.; Ferrer, I. M.; Peters, J. C.; Jaramillo, T. F. Benchmarking nanoparticulate metal oxide electrocatalysts for the alkaline water oxidation reaction. *J. Mater. Chem. A* **2016**, *4*, 3068−3076.
(73) McCrory, C. C. L.; Jung, S.; Peters, J. C.; Jaramillo, T. F. Benchmarking Heterogeneous Electrocatalysts for the Oxygen Evolution Reaction. *J. Am. Chem. Soc.* **2013**, *135*, 16977−16987.
(74) Lin, Y.; Tian, Z.; Zhang, L.; Ma, J.; Jiang, Z.; Deibert, B. J.; Ge, R.; Chen, L. Chromium-ruthenium oxide solid solution electrocatalyst for highly efficient oxygen evolution reaction in acidic media. *Nat. Commun.* **2019**, *10*, 162.
(75) Frydendal, R.; Paoli, E. A.; Knudsen, B. P.; Wickman, B.; Malacrida, P.; Stephens, I. E. L.; Chorkendorff, I. Benchmarking the Stability of Oxygen Evolution Reaction Catalysts: The Importance of Monitoring Mass Losses. *ChemElectroChem* **2014**, *1*, 2075−2081.
(76) Ye, Z.; Zhang, P.; Lei, X.; Wang, X.; Zhao, N.; Yang, H. Iron Carbides and Nitrides: Ancient Materials with Novel Prospects. *Chem.−A Eur. J.* **2018**, *24*, 8922−8940.
(77) Bao, F.; Kemppainen, E.; Dorbandt, I.; Bors, R.; Xi, F.; Schlatmann, R.; van de Krol, R.; Calnan, S. Understanding the Hydrogen Evolution Reaction Kinetics of Electrodeposited Nickel-Molybdenum in Acidic, Near-Neutral, and Alkaline Conditions. *ChemElectroChem* **2021**, *8*, 195−208.
(78) Shinagawa, T.; Garcia-Esparza, A. T.; Takanabe, K. Insight on Tafel slopes from a microkinetic analysis of aqueous electrocatalysis for energy conversion. *Sci. Rep.* **2015**, *5*, 13801.
(79) Mahmood, N.; Yao, Y.; Zhang, J.-W.; Pan, L.; Zhang, X.; Zou, J.-J. Electrocatalysts for Hydrogen Evolution in Alkaline Electrolytes: Mechanisms, Challenges, and Prospective Solutions. *Adv. Sci.* **2018**, *5*, No. 1700464.
(80) Saad, A.; Cheng, Z.; Zhang, X.; Liu, S.; Shen, H.; Thomas, T.; Wang, J.; Yang, M. Ordered Mesoporous Cobalt−Nickel Nitride Prepared by Nanocasting for Oxygen Evolution Reaction Electrocatalysis. *Adv. Mater. Interfaces* **2019**, *6*, No. 1900960.
(81) Stern, L.-A.; Feng, L.; Song, F.; Hu, X. Ni2P as a Janus catalyst for water splitting: the oxygen evolution activity of Ni2P nanoparticles. *Energy Environ. Sci.* **2015**, *8*, 2347−2351.
(82) Friebel, D.; Louie, M. W.; Bajdich, M.; Sanwald, K. E.; Cai, Y.; Wise, A. M.; Cheng, M.-J.; Sokaras, D.; Weng, T.-C.; Alonso-Mori, R.; Davis, R. C.; Bargar, J. R.; Nørskov, J. K.; Nilsson, A.; Bell, A. T. Identification of Highly Active Fe Sites in (Ni,Fe)OOH for Electrocatalytic Water Splitting. *J. Am. Chem. Soc.* **2015**, *137*, 1305−1313.
(83) Li, G.; Yang, Q.; Rao, J.; Fu, C.; Liou, S.-C.; Auffermann, G.; Sun, Y.; Felser, C. In Situ Induction of Strain in Iron Phosphide (FeP2) Catalyst for Enhanced Hydroxide Adsorption and Water Oxidation. *Adv. Funct. Mater.* **2020**, *30*, No. 1907791.
(84) Lee, J. H.; Kattel, S.; Wang, Y.; Tackett, B. M.; Xie, Z.; Hwang, S.; Denny, S. R.; Xu, W.; Chen, J. G. Prussian blue analogues as platform materials for understanding and developing oxygen evolution reaction electrocatalysts. *J. Catal.* **2021**, *393*, 390−398.
(85) Ding, X.; Li, W.; Kuang, H.; Qu, M.; Cui, M.; Zhao, C.; Qi, D.-C.; Oropeza, F. E.; Zhang, K. H. L. An Fe stabilized metallic phase of NiS2 for the highly efficient oxygen evolution reaction. *Nanoscale* **2019**, *11*, 23217−23225.
(86) Li, S.; Ren, P.; Yang, C.; Liu, X.; Yin, Z.; Li, W.; Yang, H.; Li, J.; Wang, X.; Wang, Y.; Cao, R.; Lin, L.; Yao, S.; Wen, X.; Ma, D. Fe5C2 nanoparticles as low-cost HER electrocatalyst: the importance of Co substitution. *Sci. Bull.* **2018**, *63*, 1358−1363.
(87) Pell, W. G.; Zolfaghari, A.; Conway, B. E. Capacitance of the double-layer at polycrystalline Pt electrodes bearing a surface-oxide film. *J. Electroanal. Chem.* **2002**, *532*, 13−23.
(88) Łukaszewski, M.; Soszko, M.; Czerwiński, A. Electrochemical Methods of Real Surface Area Determination of Noble Metal Electrodes − an Overview. *Int. J. Electrochem. Sci.* **2016**, *11*, 4442−4469.

https://doi.org/10.1021/acs.inorgchem.2c01713
Inorg. Chem. 2022, 61, 13836−13845